



AFRL-AFOSR-UK-TR-2013-0050



Investigation of mesospheric metal emission signals from SCIAMACHY limb measurements

***Martin Langowski, *John P. Burrows,
Christian von Savigny, *Art C. Aikin**

*** Institute of Environmental Physics, University of Bremen, Otto-
Hahn-Allee 1, Bremen, 28359 Germany;
**Institute of Physics, Ernst-Moritz-Arndt University of Greifswald,
Greifswald, Germany;
*** The Catholic University of America, Washington D.C.**

EOARD Grant 09-3012

Report Date: October 2013

Final Report from 1 March 2009 to 31 August 2013

Distribution Statement A: Approved for public release distribution is unlimited.

**Air Force Research Laboratory
Air Force Office of Scientific Research
European Office of Aerospace Research and Development
Unit 4515 Box 14, APO AE 09421**

REPORT DOCUMENTATION PAGE				Form Approved OMB No. 0704-0188	
Public reporting burden for this collection of information is estimated to average 1 hour per response, including the time for reviewing instructions, searching existing data sources, gathering and maintaining the data needed, and completing and reviewing the collection of information. Send comments regarding this burden estimate or any other aspect of this collection of information, including suggestions for reducing the burden, to Department of Defense, Washington Headquarters Services, Directorate for Information Operations and Reports (0704-0188), 1215 Jefferson Davis Highway, Suite 1204, Arlington, VA 22202-4302. Respondents should be aware that notwithstanding any other provision of law, no person shall be subject to any penalty for failing to comply with a collection of information if it does not display a currently valid OMB control number. PLEASE DO NOT RETURN YOUR FORM TO THE ABOVE ADDRESS.					
1. REPORT DATE (DD-MM-YYYY) 31 October 2013		2. REPORT TYPE Final Report		3. DATES COVERED (From – To) 1 March 2009 – 31 August 2013	
4. TITLE AND SUBTITLE Investigation of mesospheric metal emission signals from SCIAMACHY limb measurements				5a. CONTRACT NUMBER FA8655-09-1-3012	
				5b. GRANT NUMBER Grant 09-3012	
				5c. PROGRAM ELEMENT NUMBER 61102F	
				5d. PROJECT NUMBER	
6. AUTHOR(S) *Martin Langowski *John P. Burrows **Christian von Savigny ***Art C. Aikin				5d. TASK NUMBER	
				5e. WORK UNIT NUMBER	
7. PERFORMING ORGANIZATION NAME(S) AND ADDRESS(ES) * Institute of Environmental Physics, University of Bremen, Bremen, Germany **Institute of Physics, Ernst-Moritz-Arndt University of Greifswald, Greifswald, Germany ***The Catholic University of America, Washington D.C.				8. PERFORMING ORGANIZATION REPORT NUMBER N/A	
9. SPONSORING/MONITORING AGENCY NAME(S) AND ADDRESS(ES) EOARD Unit 4515 APO AE 09421-4515				10. SPONSOR/MONITOR'S ACRONYM(S) AFRL/AFOSR/IOE (EOARD)	
				11. SPONSOR/MONITOR'S REPORT NUMBER(S) AFRL-AFOSR-UK-TR-2013-0050	
12. DISTRIBUTION/AVAILABILITY STATEMENT Distribution A: Approved for public release; distribution is unlimited.					
13. SUPPLEMENTARY NOTES					
14. ABSTRACT This project developed and tested a novel retrieval algorithm to investigate mesospheric metal emission signals from SCIAMACHY limb measurements. The spectra from the SCIAMACHY limb MLT measurements (from 2008-2012) revealed number densities for several metal atom and ion species (Mg, Mg+ and Na). Through advancements in the retrieval algorithms such as the addition of a ring effect correction and the treatment of self-absorption, high-resolution features in the spectra, like fully resolved Fraunhofer lines in the solar spectrum, spectral shifts and splittings due to hyper-fine structure, Doppler effect, and isotopic compositions are now possible. As a result, the Mg vertical profiles do not show a second maximum at 70km anymore and through the improved resolution in the peak region of the metal atom and ion layers a clear latitudinal dependence of the Mg+ peak altitude could be observed for the first time. Furthermore, a treatment of multiple scattering effects extended the retrieval algorithm to derive Na densities. Knowing the global mesospheric metal density distribution, combined with models, including reaction rates of loss processes as well as the meteoric composition and fraction ablated in the upper atmosphere, enables estimating the daily input of meteoric material to the earth atmosphere. The knowledge won from the MLT dataset can be used to reanalyze the nominal limb and nadir dataset, e.g. as a priori information in the retrieval and the potential of the SCIAMACHY dataset is still not fully exhausted. An accurate neutral and ionized metals global data set is now available for the period 2008 to 2012. These data have been compared with a 2D photochemical/dynamical model for Mg and Mg+ showing that there are differences between model and data for Mg on a seasonal basis even though Mg+ model and data are in agreement. The data show clearly significant transport of both Mg and Mg+ above 100km in both the polar and equatorial regions. In addition to providing a global data set for Mg and Mg+ and Na, the present effort has demonstrated the algorithm necessary to yield the global distribution of other metal species such as Fe.					
15. SUBJECT TERMS EOARD, atmospheric chemistry, atmospheric emission, SCIAMACHY, mesospheric metal emission					
16. SECURITY CLASSIFICATION OF:			17. LIMITATION OF ABSTRACT SAR	18, NUMBER OF PAGES 35	19a. NAME OF RESPONSIBLE PERSON Kevin Bollino
a. REPORT UNCLAS	b. ABSTRACT UNCLAS	c. THIS PAGE UNCLAS			19b. TELEPHONE NUMBER (Include area code) +44 (0)1895 616163

Award # FA8655-09-1-3012 – Investigation of mesospheric metal
emission signals from SCIAMACHY
limb measurements (Mar 2010 - Oct 2013) – Final Report

Submitted by

Martin Langowski¹, John P. Burrows¹, Christian von Savigny^{1,2} and Art C. Aikin³

¹ *Institute of Environmental Physics, University of Bremen, Bremen, Germany*

² *Institute of Physics, Ernst-Moritz-Arndt University of Greifswald, Greifswald, Germany*

³ *The Catholic University of America, Washington D.C.*

Submitted on October 31. 2013

Contact:

Institute of Environmental Physics

University of Bremen

P. O. box 33440

28334 Bremen

Germany

burrows@iup.physik.uni-bremen.de

Contents

List of figures	1
1 Summary	2
2 Publications arising from the Project	3
3 Introduction	3
4 Methods, assumptions and procedures	6
4.1 Retrieval of slant column densities	7
4.2 Retrieval of densities	11
4.3 Extension for the visible spectral region	14
5 Results and Discussion	16
5.1 Results for Mg	16
5.2 Results for Mg ⁺	19
5.3 Results for Na	22
5.4 Other metals	26
6 Conclusions	27
7 Acknowledgements	28
8 Conference Contributions	30
9 List of Symbols, Abbreviations, and Acronyms	30
10 Appendix A	32

List of Figures

4.1 Ring effect correction	8
4.2 Ring effect smoothing function	8
4.3 Retrieval of slant column emissions	9
4.4 Mg ⁺ solar spectrum	10
4.5 Emissivity	11
4.6 Path calculation sketch	12
4.7 Path calculation example result	13
4.8 Na slant column densities	15
4.9 Optimal albedo factor	15
5.1 Mg monthly means	17
5.2 Mg seasonal variations	18
5.3 Mg annual mean	19
5.4 Mg ⁺ monthly means	20
5.5 Mg ⁺ seasonal variations	21
5.6 Mg ⁺ annual mean	22

5.7	Na D1 monthly means	23
5.8	Na D2 monthly means	24
5.9	Na D1-D2 monthly means	25
5.10	Na VCD vs latitude and month	26
5.11	Fe 372 nm line	27

1 Summary

The overall objective in the SciaMetals III project has been to use the limb measurements made by SCIAMACHY (SCanning Imaging Absorption spectroMeter for Atmospheric CHartographY), which flew on the European Space Agency's satellite Envisat, to investigate the content and variability of metal species in the mesosphere and lower thermosphere (MLT). Dayglow emission signals of the metal atoms and ions are detected in the observation of scattered electromagnetic radiation made by the grating spectrometer SCIAMACHY. The emission signals are separated from the radiation scattered back to space by the atmosphere or the earth's surface. A mathematical algorithm, which uses a forward atmospheric radiative transfer model, was developed to invert the observed emissions into densities of the metal atoms and ions as a function of altitude and latitude. SciaMetals III builds on a previous project and provides the first opportunity to investigate measurements from the MLT-mode of SCIAMACHY. It was established after the findings from the SciaMetals I and II projects, that it would be valuable to observe the region from 90 to 140 km in more detail. In addition to the nominal SCIAMACHY limb scans with tangent altitudes from ground up to 93 km, which have been continuously performed from 2002 until the unexpected loss of Envisat in April 2012, the MLT-mode observes the 50 to 150 km altitude region in 30 3.3 km steps. These measurements include the maximum density region of the metal atoms and ions and were performed from mid 2008 until April 2012 producing 84 single days of data (one day every two weeks). In addition to the exploitation of this new source of data, several improvements were implemented in the radiative transfer model:

- i) A simple but effective correction for the filling-in of Fraunhofer lines by inelastic Raman scattering (Ring effect) was developed. This was validated by comparison with a more rigorous and computationally expensive algorithm (SCIATRAN).
- ii) A physical description of the self absorption of the electromagnetic radiation emitted by the metal atoms and ions was developed.
- iii) High resolution solar spectra to calculate the emissivity and species dependent hyperfine structure splitting and isotope shifts of the atomic and ion lines are used now.
- iv) An approach to account for Doppler shifts between sun and earth and solar red shift of the Fraunhofer lines have been developed.
- v) A novel approach to account for the backscattered/reflected light from the surface and lower atmosphere in the visible region is now implemented in the retrieval.

A detailed description of the new retrieval algorithm applied to Mg and Mg^+ , with an error estimation and sensitivity studies on critical parameters has been already been published in Atmospheric Measurement Techniques Discussions (AMTD). It is now in final revision for acceptance in Atmospheric Measurement Techniques (AMT). A publication discussing the results of Mg and Mg^+ for the 4 year MLT dataset will be submitted shortly. The new results for sodium atoms are in good agreement with those obtained from other in-

struments and another manuscript on the extension of the retrieval algorithm as well as the Na results itself will be submitted for publication. An adapted version of the retrieval code developed in the Sciametals-projects was used at KIT, in cooperation with our group, to derive the mesospheric and lower thermospheric content of NO from SCIAMACHY, which resulted in a publication in AMTD/AMT [2] so far, and further publications are already in preparation. Finally a survey of the atmospheric emission features observed by SCIAMACHY has also been undertaken.

2 Publications arising from the Project

M. Langowski, M. Sinnhuber, A. C. Aikin, C. von Savigny, and J. P. Burrows, Retrieval algorithm for densities of mesospheric and lower thermospheric metal and ion species from satellite borne limb emission signals, *Atm. Meas. Tech. Disc.*, Vol. 6, No 3, Pages 4445-4509, 2013.

Publications in Preparation:

M. Langowski, C. von Savigny, J. P. Burrows, W. Feng, J. M. C. Plane, D. R. Marsh, D. Janches, M. Sinnhuber and A. C. Aikin, Global Mg and Mg ion observation between 70 km and 150 km with SCIAMACHY/Envisat, *J. of Atmos. and Sol.-Terr. Phys.*, to be submitted in Nov 2013.

Atmospheric Sodium profiles, retrieved from SCIAMACHY limb observations

A survey of the emission features observed in the SCIAMACHY limb spectra

3 Introduction

During its orbit around the sun, the earth and its atmosphere passes through the solar system dust. As a result, meteoroids enter the earth's atmosphere and ablate. Two sources of the meteoroids have been identified (see, e.g. [3]). The first results from the comet trails of comets that pass closely by the earth on time scales on the order of 100 years. The earth passes through or close to these meteor streams at around the same time each year, e.g. the Perseids around the 12th August. Although the meteor showers may indicate that the input of meteoric material may increase during these events, they are a minor source of total meteoric input. Measurements (e.g. [4], [19]) show, that the amount of meteoric material entering the atmosphere does not significantly change during meteor showers. However, the impact of these showers on the upper atmosphere is nevertheless observed (e.g. [10]). The other source of meteoric input are trails from long decayed comets and dust from the asteroid belt between the orbit of Mars and Jupiter. In [15] it is claimed that more than 90% of the meteoric mass entering the earth atmosphere comes from the Jupiter Family Comets.

The total daily mass input of meteoric material is still uncertain and estimates range from 2 to 300 tons of material (see, e.g. [16]). The meteoroids enter the atmosphere not because of the earth's gravity, but because of the ballistic collision at the crossing point of

the orbits of both earth and meteoroid around the sun. This leads to high entry velocities of the meteoroids, typically being equal to or greater than 11.2 km/s, which is the escape velocity from the earth's gravity field. Meteoroids entering the atmosphere collide with air molecules, which leads to deceleration and frictional heating of the meteoroids. This in turn eventually produces ablation of the meteoroids. The vertical location of the ablation depends on the meteoroids mass, composition, entry velocity and entry angle as well as the melting point of its constituents. In addition, the meteoroids produce shock waves due to their hypersonic speeds. Qualitatively, the following scenarios describe the entry of meteoroids into the atmosphere (see, e.g. [3]): Some meteoroids are small enough, that they decelerate fast enough and not become hot enough to melt. These meteoroids can be detected by impact craters on satellites or ground. However, since the meteoroid material does not show any signs of melting it can not be distinguished from earth materials. A different type of meteoroid contributes to dust in the upper atmosphere. As a result of collisions with air molecules, i.e frictional deceleration, the meteoroid heats up rapidly enough to ablate. Under typical conditions this happens between 85 and 105 km altitude. The heated material also emits radiation to loose energy. This can be seen as a trail of ablated material behind the meteoroid. This emission by the trail is called a meteor. Meteoroids and trails can be detected with radar. The meteoroids can fully ablate. They also can decelerate fast enough, that they survive the ablation process. In this case they cool down quickly, which leads to a "dark flight" with no emission. The particle falls down to earth at the (subsonic) free fall velocity, limited by friction. Large meteoroids are not decelerated fast enough and hit the surface with supersonic velocities. Meteoroids which hit the surface are called meteorites. This behavior is identified by the melted surfaces of meteorites. As a result of the large range of meteoroid sizes (see, e.g. [7], for a meteoroid size distribution) and the different time scales over which meteoroids of different sizes have to be observed, a single instrumental technique is not capable of measuring all the meteoroids. This is one reason why the magnitude of the daily input of meteoroids remains uncertain.

Metal atoms are ablated from the meteoroids in an altitudes between approximately 85 and 105 km in the vicinity of the mesopause. A fraction of the metals is ionized by the hyperthermal collisions with the air molecules ([20]). In addition, metal atoms are ionized by charge exchange reactions with O_2^+ and NO^+ (see, e.g. [17], [1]). The most reactive species in this altitude is O_3 and reaction with O_3 reduces both the metal atom and ion density. This leads to metal oxides, hydroxides and carbonates, which condense and form meteoric smoke particles. These meteoric smoke particles sink and can contribute as nuclei to the heterogenous condensation required to form clouds. The metal atom and ion clusters thus represent a source of condensation nuclei for the formation of polar mesospheric clouds in summer. Their chemistry interacts with the chemistry of ozone in the summer mesosphere. As they descend into the stratosphere the metal atom and ion clusters may also be condensation nuclei for polar stratospheric clouds in winter and spring at high latitudes and have an impact on the chemistry of stratospheric ozone. After entry into the troposphere, the metals and their compounds are eventually deposited at the surface by wet or dry deposition.

The mesosphere and lower thermosphere is difficult to probe with in-situ instrumentation. The air density there is too low for aircraft and balloons to fly in, while the air density is too high for satellites to orbit because of the very high drag. Instruments carried

by rockets are used to investigate the composition of this region. However, rockets can only be launched from a limited number of locations and rocket flights have a limited duration preventing continuous time coverage and are expensive. Therefore, there are only few in situ measurements of metal atoms and ions available. In addition, these measurements were performed under special atmospheric conditions.

The metal atoms and ions are strong emitters of dayglow radiation produced by resonance fluorescence of solar light. The emissions can be well detected, despite the small densities of the metals and metal ions, which are on the order of 10 to 10^4 particles per cubic centimeter. In the near UV and visible spectrum the atom lines of Fe, Na, K and Ca are observed by lidar instruments from ground, which have a good vertical and temporal resolution. Valuable information on mesospheric temperatures, wind speeds and wave propagation effects into the upper atmosphere are retrieved by this technique. However, the number of lidar sites is very limited and the measurements are thus sparse. Measurements by passive remote sensing instrumentation from orbiting satellite platforms provide global coverage of the metal atom and ion emissions, but typically have poorer vertical resolution than the measurements retrieved by lidar. In addition, one advantage of space based observations is that the emission lines in the UV region, e.g. for Mg and Mg^+ , where the strong absorption of radiation by ozone limits access from the ground, are readily observed.

In this project we use spectrometric measurements made by the SCIAMACHY instrument on the Envisat satellite and retrieve number densities of metal atoms and ions. Envisat was launched in spring 2002 and hosts several scientific instruments. In April 2012 ESA lost communication with Envisat. Envisat flies in a sun synchronous polar orbit in descending node, having an altitude around 775 km and an equator crossing time of 10 a.m..

One of the instruments on Envisat is the grating spectrometer SCIAMACHY. This instrument is a double monochromator and it measures the back scattered and reflected radiation upwelling from the top of the atmosphere in nadir and limb viewing geometries and both solar and lunar occultation. After collection, the electromagnetic radiation is measured in 8 spectral channels. The first 6 channels measure continuously from 214 to 1750 nm wavelength, having a spectral resolution of ≈ 0.22 nm in channel 1 (200 - 300 nm) and ≈ 0.44 nm in channel 3 (400 - 600 nm). Channel 7 and 8 make measurements in two short-wave infrared bands from 1940 to 2040 nm and 2260 nm to 2380 nm, respectively. The wavelength of the strongest resonant emission lines from the lowest excited state to the ground state of several metal atom and ion species are found in this region (e.g. Fe at 248 and 372 nm, Mg at 285 nm, Mg^+ double line at 280 nm, Ca at 422 nm, Ca^+ at 393 and 396 nm, Na double line at 589 nm and K at 770 nm). SCIAMACHY scans the electromagnetic radiation leaving the atmosphere in limb, nadir and occultation mode.

In the occultation mode the instrument points directly through the atmosphere at an electromagnetic radiation source, e.g. the sun or the moon (other instruments like GOMOS/Envisat also point at stars). Furthermore, the extraterrestrial solar spectrum (occultation without earth atmosphere between satellite and sun) is measured by SCIAMACHY once per orbit, and the solar spectral irradiance is estimated. The retrieval of profiles is relatively simple for the occultation measurements. This is because to a first order approximation only absorption, governed by the Beer-Lambert-law needs to be considered. However, the SCIAMACHY instrument, which flies in a sun synchronous orbit,

has only one solar occultation measurement per orbit close between 60 and 80°N latitude dependent on season and lunar occultation for around 6 days a month close to full moon for 6 months of the year without solar illumination between 60 and 80°S.

In nadir mode (nadir is the opposite direction to zenith) the satellite points towards the earth surface with a maximum zenith angle of 30°. The nadir mode of observation achieves global coverage at the equator in 6 days. However, only column information can be measured in this mode and in most cases assumptions on the vertical structure of the measured species have to be used as input information to retrieve the true vertical columns from the measured slant columns.

In limb mode the satellite points tangentially to the earth surface. This is done for several tangent altitude steps. In the nominal limb mode 30 scan from -2 km to 93 km tangent altitude with 3.3 km step size are performed and there is an additional measurement at 250 km altitude for dark current corrections (assuming that the signal should be zero there). In a typical SCIAMACHY orbit sequence limb and nadir modes are alternatively used, so that both can be combined through a limb-nadir-matching of measurements covering the same air volume. This alternative pattern is switched every other orbit, to close the gaps in the latitudinal coverage of both modes, that occurs when the other mode is used. On the day side of an orbit, which lasts approximately 100 minutes, roughly 30 sets of limb measurements and 30 sets of nadir measurements are performed.

During the early period of SCIAMACHY until spring 2003 nominal limb scans were performed up to 105 km tangent altitude. However, in a trade-off for a better limb-nadir-matching and to improve the O₃ retrieval, the vertical coverage was reduced.

From the middle of 2008 until April 2012 an additional limb MLT mode was performed, which was established specially for the observation and investigation of trace species with pronounced maxima in the number density in the MLT region, like the metal atoms and ions, or NO. This mode runs for 15 consecutive orbits (1 day of data) every 14 days. The limb MLT scans replaced the nominal limb scans for these days. This resulted in 84 days of limb MLT data. In the limb MLT scans the lowest tangent altitude is set to 53 km, while the step size is still the same and the highest covered altitude is 150 km. The additional dark current scan is shifted upwards to 350 km altitude.

4 Methods, assumptions and procedures

A detailed description of the retrieval algorithm for Mg and Mg⁺ developed in this study can be found in [11], and only a shorter version of this is presented here. In addition, the improvement of the correction developed to account more precisely for the solar scattered electromagnetic radiation entering the instrument field of view, iFOV, and used in the Na retrieval is presented.

The retrieval algorithm can be divided in two separate retrieval steps. First the slant column density profiles are retrieved from the SCIAMACHY spectral observations, then the number densities of metal atoms and ions are retrieved from the slant column density profiles, resulting in a vertical profile of the targeted metal atom or ion.

4.1 Retrieval of slant column densities

The Mg line lies at 285.2 nm and the Mg⁺ lines lie at 279.6 and 280.4 nm. To reduce the noise of the SCIAMACHY data in this wavelength region, we average the spectral data at collocated latitudes and local times for the 15 orbits of the MLT measurements of one day. The probability that the spectral line fit fails, which would lead to additional systematic errors, is reduced by averaging the data. Furthermore, the statistical error of the slant column densities is reduced. This also reduces a source of systematic noise as the noise from the electromagnetic backscattered solar radiation would result in a bias to higher densities.

The first step in the retrieval of the slant column densities is to separate the emission signal from the backscattered solar radiation and instrument signal, which is called the background signal. This background signal is attributed predominantly to resonant Rayleigh scattering and non-resonant Raman scattering. The Rayleigh spectrum is an attenuated transformation of the solar spectrum, modulated with a phase function and an attenuation, which has a wavelength dependence of λ^{-4} . For small wavelength windows of 1 nm width (at ≈ 300 nm wavelength) the ratio of the Rayleigh background divided by the solar spectrum can be well approximated as a straight line. The non-resonant Raman scattering is important for spectral regions with large gradients in the solar spectrum, e.g. Fraunhofer lines. Since the metals in the MLT are also found in the solar atmosphere, the metal lines always coincide with solar Fraunhofer lines. This happens because the absorption by the metals in the solar atmosphere is the reason for the Fraunhofer line. Scattering is stronger, where the intensity is higher and, therefore, effectively more electromagnetic radiation is scattered from wavelength regions with high intensity to regions with lower intensity than vice versa. This leads to a filling in of Fraunhofer lines which is called Ring effect [8]. The atmospheric emission have a narrower full width half maximum, FWHM, than the solar Fraunhofer lines, because the temperature of the upper atmosphere is much lower than that of the sun and the solar Fraunhofer lines are additionally broadened by pressure broadening.

The Ring effect is corrected in the following way. The Ring effect is applied to the Ring effect affected spectrum I_1 a second time to obtain the spectrum I_2 . Assuming that the effect is small and linear when applied a second time, the unaffected spectrum I_0 is found by subtracting the difference of I_1 and I_2 from I_1 .

$$I_2(\lambda) = I_1(\lambda) + \underbrace{\Delta I_{R2}(\lambda)}_{I_2(\lambda) - I_1(\lambda)} \quad (4.1)$$

$$I_1(\lambda) = I_0(\lambda) + \underbrace{\Delta I_{R1}(\lambda)}_{I_1(\lambda) - I_0(\lambda)} \quad (4.2)$$

Under the assumption $\Delta I_R(\lambda) = \Delta I_{R2}(\lambda) = \Delta I_{R1}(\lambda)$ it follows that

$$I_0(\lambda) = I_1(\lambda) - \Delta I_R = 2I_1(\lambda) - I_2(\lambda). \quad (4.3)$$

To test whether this linearization approach works, the Ring effect is applied to I_0 , which results in I_1 again. Figure 4.1 shows I_0 , I_1 , I_2 and I_1 recalculated from I_0 for a sample spectrum. Both I_1 in Fig. 4.1 are nearly identical. The smoothing function which is applied as the Ring effect operator is shown in Fig. 4.2.

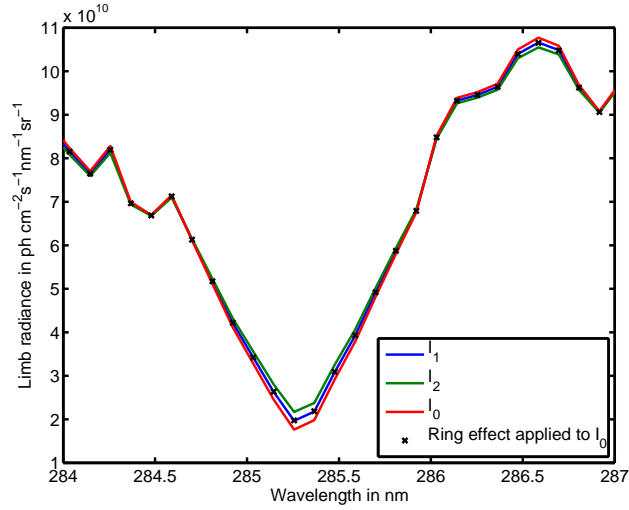


Fig. 4.1: Ring effect correction for the Mg 285.2 nm line, for a limb measurement with a tangent altitude of 53.5 km. The Ring effect is simulated using the measured spectrum $I_1(\lambda)$ to obtain $I_2(\lambda)$. The filling-in effect is assumed to be small and differences between the first and the second application are therefore also small. Under this assumption the differences are the nearly the same $I_0(\lambda) - I_1(\lambda) \approx I_1(\lambda) - I_2(\lambda)$. And by adding $I_1(\lambda)$ the corrected spectrum $I_0(\lambda)$ is obtained as $I_0(\lambda) = 2I_1(\lambda) - I_2(\lambda)$.

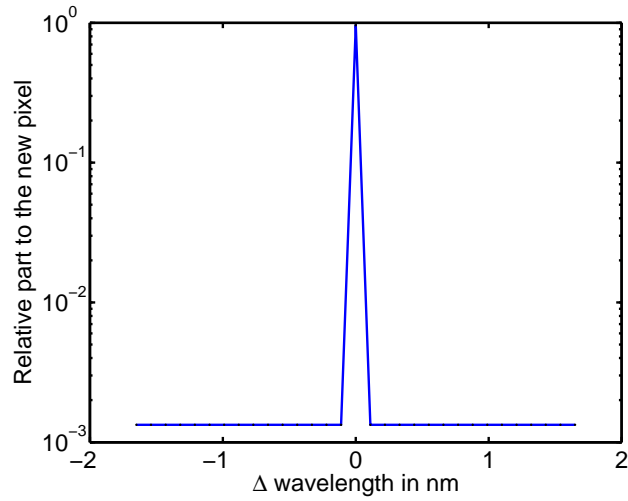


Fig. 4.2: Ring effect smoothing function. 96% of the background light is Rayleigh scattered. The Raman scattered part is approximated by a boxcar for the remaining 4%.

We compared this empirical Ring effect correction with the more sophisticated and physical accurate approach used within SCIATRAN [18]. The two approaches are in good agreement for the Mg/Mg⁺ lines. However, in regions where the Ring effect filling-in is much larger than the actual emission signal, the simpler and computer efficient correction

is not sufficient. Therefore the region below 70 km is excluded of the application of this retrieval algorithm.

After the Ring effect correction, the remaining background signal from Rayleigh scattering is subtracted as explained below: The limb spectrum is divided by the solar spectrum. A linear fit in the vicinity of the emission line is applied to this spectrum, which however, excludes the wavelength window of the emission line. This linear fit is subtracted from the spectrum and the solar spectrum is multiplied again, to obtain the pure limb emission spectrum. The pure limb emission spectrum is then fitted with a single line fit for Mg and a double line fit for Mg^+ , to obtain the the slant column emission. These steps are illustrated for Mg in Fig. 4.3.

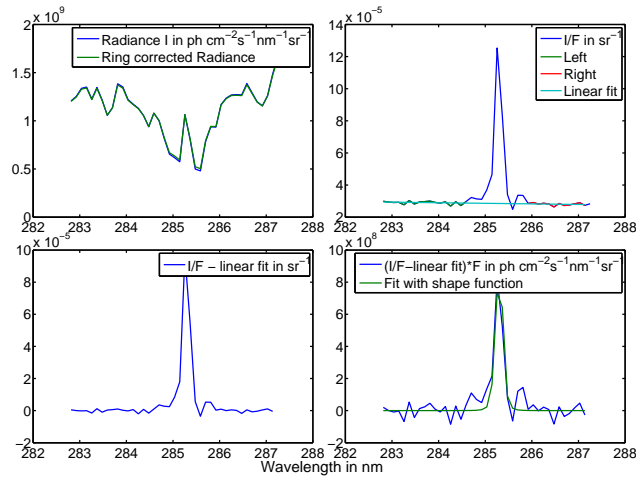


Fig. 4.3: Slant column emission determination. First the Ring effect correction is applied to the limb radiance I (top left). The limb radiance is divided by the solar irradiance F and the wavelength region left and right to the line are used for a linear fit of the background radiation (top right). The linear fit is subtracted from the ratio I/F (bottom left) and the spectrum is again multiplied with the solar irradiance F (bottom right). Finally the area of the emission line is fitted with the slit function of the instrument.

Assuming single scattering of light from the sun into the LOS of the instrument (emission path s_e), for a single measurement (one limb spectrum at one altitude) the forward model for the slant column emission can be calculated as follows:

$$4\pi I = \int_{LOS} \gamma n(s_e) f(\int n(s_a) ds_a) ds_e \quad (4.4)$$

with emissivity γ , density n and an absorption part – along the LOS and the line from sun (LFS) (s_a stands for both absorption paths) – f . In the first step of the retrieval the left hand side of Eq. (4.4) is determined, while in the second step the right hand side of Eq. (4.4) is inverted to obtain the density n . The slant column density is

$\int_{LOS} n(s_e) f(\int n(s_a) ds_a) ds_e$, so equation 4.4 has to be divided by the emissivity γ .

$$\underbrace{\gamma}_{\frac{\text{photons}}{s}} = \underbrace{P(\theta)}_{\text{Phase function}} \cdot \underbrace{\pi F_{\lambda_0}}_{\frac{\text{photons}}{s \text{ cm}^2 \text{ nm}}} \cdot \underbrace{\frac{1}{4\pi\epsilon_0} \frac{\pi e^2}{mc^2} f_{ij} \lambda_{ij}^2}_{\text{int. abs. cross section in nm cm}^2} \cdot \underbrace{\frac{A_{ji}}{\sum_k A_{jk}}}_{\text{rel. Einstein coeff.}} \quad (4.5)$$

Beside the phase function $P(\theta)$ all other factor in γ are independent of the integration path ds_e . For the solar irradiance πF , a high resolution spectrum has to be used, since spectrometers with low resolution smooth the Fraunhofer lines. This leads to an overestimation of πF for absorption lines (e.g. for Mg at 285.2 nm) and an underestimation for emission lines (e.g. for Mg^+ , see Fig. 4.4).

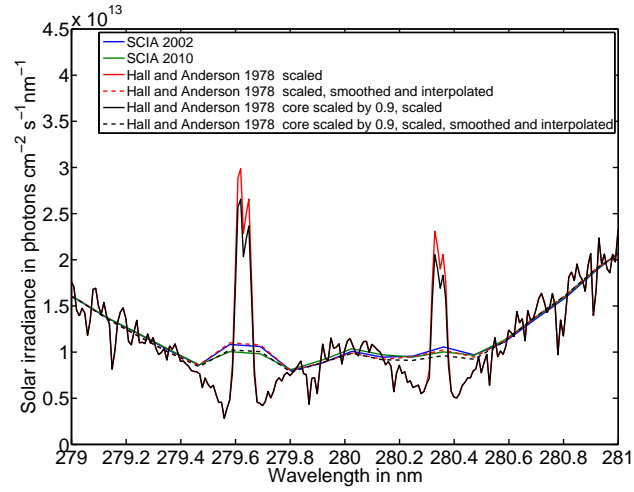


Fig. 4.4: SCIAMACHY solar spectrum in the Mg^+ double line region for low (2010) and high (2002) solar activity in comparison with the scaled high resolution reference spectrum. When the high resolution spectrum is smoothed and sampled as the SCIAMACHY spectrum there are only small differences left between both, mainly resulting from different phases of the solar cycle for the different spectra. An adjustment for the solar phase is done by scaling the core of the emission lines. The adjustment has to be done for each line individually. Possible variations of the inner structure of the the emission lines are not considered.

The high resolution spectrum was measured for one certain day in 1978, but it is known that the Fraunhofer lines vary during the solar cycle. Thus the variations in the SCIAMACHY solar spectra are considered to estimate the phase of the up to 20% variation during the 11 year cycle and the up to 10% variations during the 27 year cycle. This is done by applying different scaling factors for the core region of the emission lines of the high resolution spectrum and applying the SCIAMACHY instrument effects to it, to forward model how the SCIAMACHY spectrum looks like for different scaling factors. The inverse function of this is used to derive the needed scaling factors from the daily SCIAMACHY spectrum, which is done for each line individually. In this way the variation in the magnitude of the high resolution spectrum is considered. However, no information for

changes in the line shape of the high resolution spectrum can be derived from this, because this information is irreproducibly lost in the smoothing by the instrumental resolution function.

The non-linear function f represents the self absorption, which in the simplest case for a monochromatic wavelength obeys the Beer-Lambert-law for absorption $I = I_0 e^{-\sigma \int n ds}$, with the absorption cross section σ and the column density $\int n ds$ and intensity before and after the absorption process I_0 and I . f is the ratio of the emissivity γ after and before passing the atmosphere and can have values between 0 and 1, 1 meaning no self absorption. For the self absorption correction the wavelength dependence of σ has to be taken into account. For the calculations the wavelength integrated cross section is distributed over the Doppler-broadened shape function of the line. Small wavelength shifts for different isotopes as well as hyper-fine splitting of the line, both reducing σ in the center of the line are taken into account. For the product of the cross section in the mesosphere and the solar spectrum, Doppler shifts between sun and earth and the solar redshift have to be considered as well as isotope shifts and hyper-fine structure splittings of the lines. An illustration of the calculations for Mg is shown in Fig. 4.5.

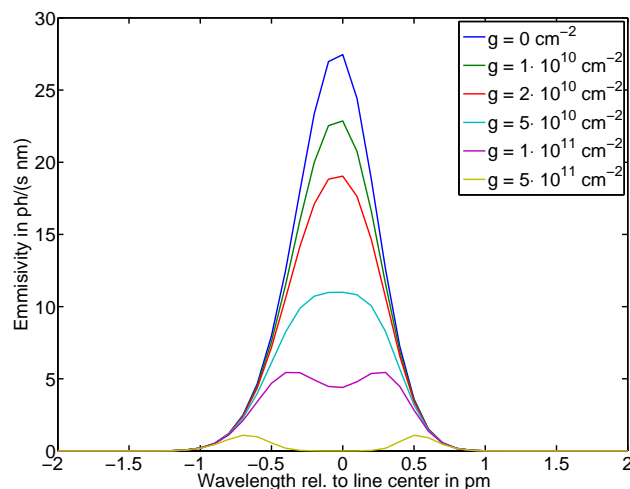


Fig. 4.5: Calculation of the wavelength specific emissivity for the Mg 285.2 nm line as a function of wavelength difference from the center of line. It is the product of solar irradiance attenuated along the LFS and the LOS and the absorption cross section. To obtain the emissivity of the spectral line, this spectrum has to be integrated over all wavelengths. For strong absorption the light comes mainly from the edges of the profile instead of the core. This reduces the effective cross section for the total integrated profile (g is the passed metal column $\int n ds$).

4.2 Retrieval of densities

The densities of metals atoms and ions are retrieved on a 2D latitude and altitude grid for all measurements of an orbit. An orbit comprising the averaged data is used as a reference orbit for the geolocations. To calculate the densities from the forward model (Eq. (4.4)), the forward model is placed discretely on the 2D grid. As a result, paths in each grid element for each measurement have to be calculated for the emission. Furthermore, path

matrices for the absorption along the line of sight and along the line from sun to the grid element have to be calculated for each grid element on the line of sight of the instrument. The vertical grid levels are calculated with right angle triangle algebra, using the right angle at the tangent point and two sides (the tangent altitude and altitude of the grid level) to calculate the distance of the grid level to the tangent point as the third side. Paths in one grid cell then are the differences of the third side for the upper and lower boundary. The changes of latitudes within a grid level can be calculated by setting the straight line equation of the line of sight with the origin at the tangent point equal to the double cone equation for latitudes. This is easy, but rather long in the source code, since many special cases have to be treated. The distances of the crossing points of latitude cones and line of sight to the tangent point are added to the distances of the vertical grid levels from tangent point. This is illustrated in figure 4.6 and the result for one exemplary limb scan are shown in figure 4.7.

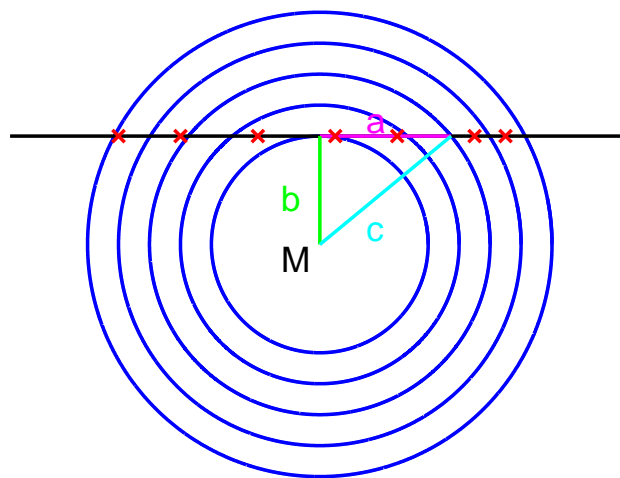


Fig. 4.6: 2D intersection of earth's atmosphere, with the center of earth M, and the altitudes as radii of the circles. Path lengths along the LOS for the vertical grid can be found with right-angled triangle algebra. Changes of the latitude in a vertical grid cell are added as additional sides a (red crosses). The path length in each grid cell is the difference of the sides a of neighboring grid cells. Note that dependent on the binning of the latitudes, it is possible, that all grid cells only have one latitude.

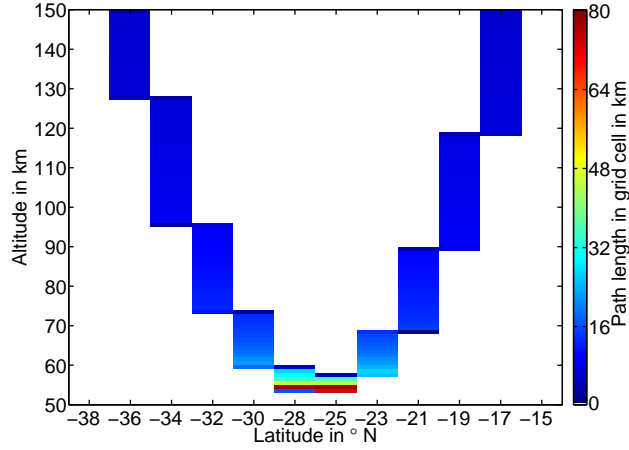


Fig. 4.7: Path lengths in different grid cells for a typical LOS of a limb measurement. The biggest part of the path lies in the tangent point altitude region, but higher altitudes are also passed.

The retrieval algorithm minimizes the difference between the forward model Kx for the slant column densities and the measured slant column densities y , finding the minimum of the sum of the squares of the differences between forward model and measurements (called χ^2), to find the best densities x . To find the minimum of χ^2 the derivative for x has to be formed and set equal to zero, This leads to the following matrix equation:

$$J^T J x = J^T y \quad (4.6)$$

with the Jacobian J which is the derivative of Kx . For the linear problem, where K is independent of x , it follows $J = K$. However, the absorption function f in the forward model in Eq. (4.4), leads to a slightly different Jacobian, which is also dependent on x . Since J is dependent on x in Eq. (4.6), which should be solved for x , an iterative approach has to be used. An initial value for x_0 in the calculation for J is used, to calculate a new x , from which J is calculated for the next iteration step etc. Since self absorption is weak, $x_0 = 0$ is a good starting point, since it gives the result without self absorption. The iteration typically converges after only a few steps and reproduces synthetic profiles well. Eq. (4.6) is the simplest equation to solve this problem. However, measurements errors must be weighted and some constraints have to be introduced to avoid strongly oscillating results, which perfectly solve the forward problem, but give physically unreasonable results. These oscillations are suppressed by a Tikhonov regularisation, which tries to minimize differences to an a priori solution (a zero density profile is used as the a priori solution). In addition, constraints minimizing the differences of neighboring grid elements for vertical and latitudinal smoothing are applied. Which leads the retrieval equation:

$$(J^T S_y J + S_a + \lambda_h S_H^T S_H + \lambda_\phi S_\phi^T S_\phi) \vec{x} = J^T S_y \vec{y} + S_a \underbrace{\vec{x}_a}_{=0} \quad (4.7)$$

with the covariance matrix of the slant column densities S_y , matrices for the a priori, vertical and latitudinal smoothing S_a , S_H , S_ϕ , scaled with different linear parameters λ ,

and the a priori solution x_a . Since x_a is zero the last addend at the right hand side is also zero. This linear equation system is solved by a LU-decomposition.

Note that a significant part computational time is spend on the calculation of the absorption paths. because this have to be done for each grid element on each measurements line of sights. This is thus done once before the retrieval iteration. The bottleneck for speed, however, is the actual iterative inversion of the forward model. Most grid elements have zero contributions to a single measurement, which leads to sparse matrices. Using sparse matrix algorithms overcomes most disadvantages in computation time for big sparse matrices, compared, e.g. to the retrieval on purely vertical grids, which uses denser matrices. Most time was saved forming some matrices directly (e.g. $\lambda_h S_H^T S_H$, in eq. (4.7)) or using block multiplication for matrix multiplication. The band-diagonal shape of the left hand side of eq. 4.7 is exploited in the inversion step.

4.3 Extension for the visible spectral region

The algorithm described above works well for spectral lines in the UV region, because only single scattered light has to be considered, and the strong ozone absorption below 290 nm justifies the single scattering approach. For the visible region multiple scattering as well as reflected light from the surface have to be considered. This effectively increases the actinic flux as a source for the metal's resonance fluorescence. The simplest approach is to estimate this increase in actinic flux as a constant factor, which we call the albedo factor. If the factor is 1 only the direct light from the sun contributes to the actinic flux, while higher factors consider multiple passing of the light through the grid elements. For similar investigation with Osiris/ODIN [9] the measured background light at 40 km tangent altitude was compared to the single Rayleigh scattering signal, to find the albedo factor as a ratio of both. However, this ratio is highly variable with altitude and yields extremely high albedo factors at altitudes above 50 km, most probably because stray light increases the measurements signal. Therefore, we used another approach, using the fact that the D1 and D2 Na lines have different absorption cross sections and are therefore differently sensitive to self absorption and the albedo factor. If the albedo factor is low, the densities are higher and there is more self absorption. If the albedo factor is high, the densities are low and there is nearly no self absorption. For the applicability of this approach it is important that the peak density is large enough that self absorption is not negligible, as is the case for the SCD profile in figure 4.8.

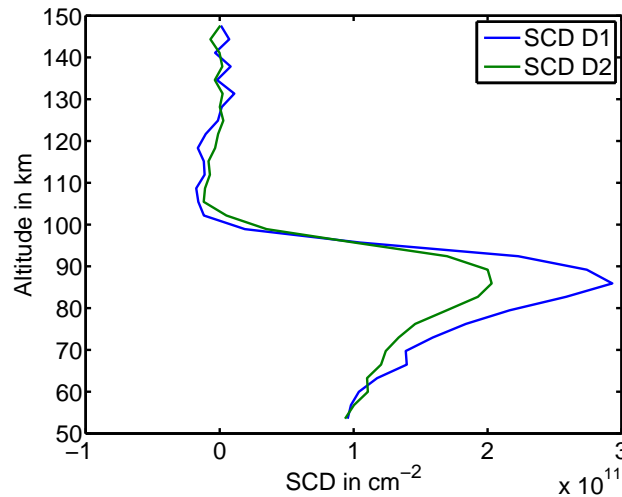


Fig. 4.8: Vertical SCD profile for Na (Summer, low latitude). The SCDs for the D1 line are larger, because the D2 line has a stronger self absorption.

Figure 4.9 demonstrates how to find the best albedo factor for the example profile. The SCDs are divided by the albedo factor and the retrieval is run. If the albedo factor is too large, the D1 line typically has a higher peak density than the D2 line, and if the albedo factor is too small, the D2 line has the higher peak density. Since peak density is sensitive to noise, we use the vertical columns between 80 and 105 km for comparing the D1 and D2 line results. The optimal albedo shows a match for those columns for D1 and D2.

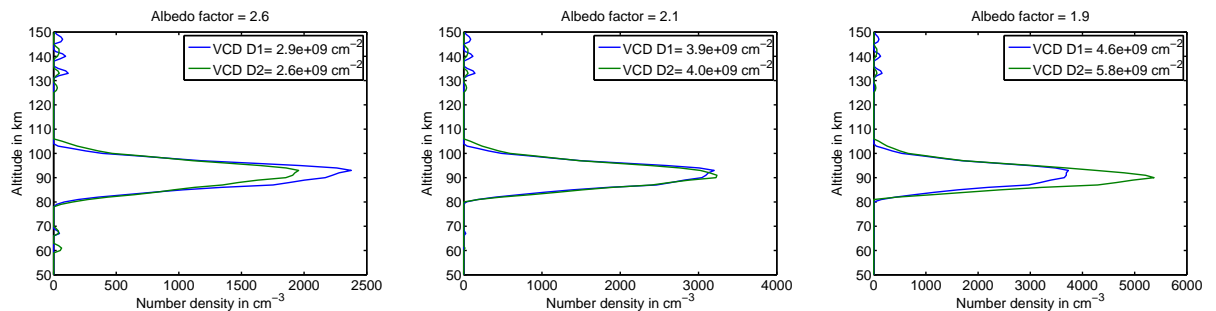


Fig. 4.9: Retrieved Na densities for the profiles shown in Fig. 4.8. For this example the albedo factor of 2.1 (mid) results in the best match for the D1 and the D2 line. For higher albedo factors (left) the inversion of the self absorption effect is too weak and the D1 densities are higher than the D2 densities, while for lower albedo factors (right) self absorption is overestimated and the D2 line yields higher densities.

For low albedo factors, the sensitivity of the D1 line and D2 line to the albedo factor switches and the D1 lines yields higher densities. Therefore a step wise search of the optimal albedo factor is necessary starting from a high albedo factor of, e.g. 3.0 in 0.1 steps, and the first local minimum in the VCD differences is investigated with smaller step sizes. This procedure is iteratively undertaken for the 1D retrieval, using a vertical grid

for the subsets of 30 measurements with the same latitude, because this is much faster than for the 2D algorithm. After finding the albedo factors for all measurements, these factor are applied in the 2D retrieval. This algorithm works for most of the measurements but some issues remain. For low densities, e.g. at high latitudes in the summer, this algorithm fails, because the self absorption is not strong enough to retrieve an optimal albedo factor. There are also measurements where the D1 SCDs are too large compared to the D2 SCDs, so that the D2 density is never larger than that of the D1 for any albedo factor, or more seldomly, the D2 SCDs are already larger than the D1 SCDs. We currently try to understand this behavior. It has to be noted that the albedo factor also affects the phase function (see equation (4.5)), because the additional multiple scattered light can be assumed to be unpolarized. Because the range of albedo factors is small, ranging from 1.0 to 3.0 for the most extreme cases, the retrieval can be run with a reference albedo factor (e.g. a constant factor, or a factor derived from the solar zenith angle etc.) that leads to best matches with collocated ground based measurements. However, it would be better to avoid this, to have independent results. Anyway, beside this issue with the absolute value of the densities, the seasonal variations, as well as the vertical profile of Na are very well retrieved with the current algorithm, producing a unique set of Na profiles for the period 2002 to 2012.

5 Results and Discussion

Results for Mg and Mg^+ have been published in [11] and will be submitted [12], where more details can be found. The results in [11] focus more on error estimations and sensitivity studies for critical parameters in the algorithm, while [12] shows the actual results for monthly means of the 4-year MLT dataset, which are also compared to model results.

The errors in the maximum density region, estimated with a Monte-Carlo method, for daily means are quite high with roughly 30% for Mg^+ and 50% for Mg. 4 to 8 daily means were averaged for each month. Furthermore, due to the high errors, the Mg/ Mg^+ retrieval is quite sensitive to different strength of the constraints and an optimal constraint can hardly be found, adding an additional uncertainty in the same order of magnitude as the statistical error, which, however, is systematic and not reduced by averaging. For Mg the error is furthermore increased at the lower peak edge, due to systematic issues with the Ring effect correction.

5.1 Results for Mg

Monthly mean results for Mg are shown in figure 5.1 and the seasonal variations for different latitudinal zones are shown in figure 5.2. Figure 5.3 shows the mean result for the 4 years of the MLT dataset.

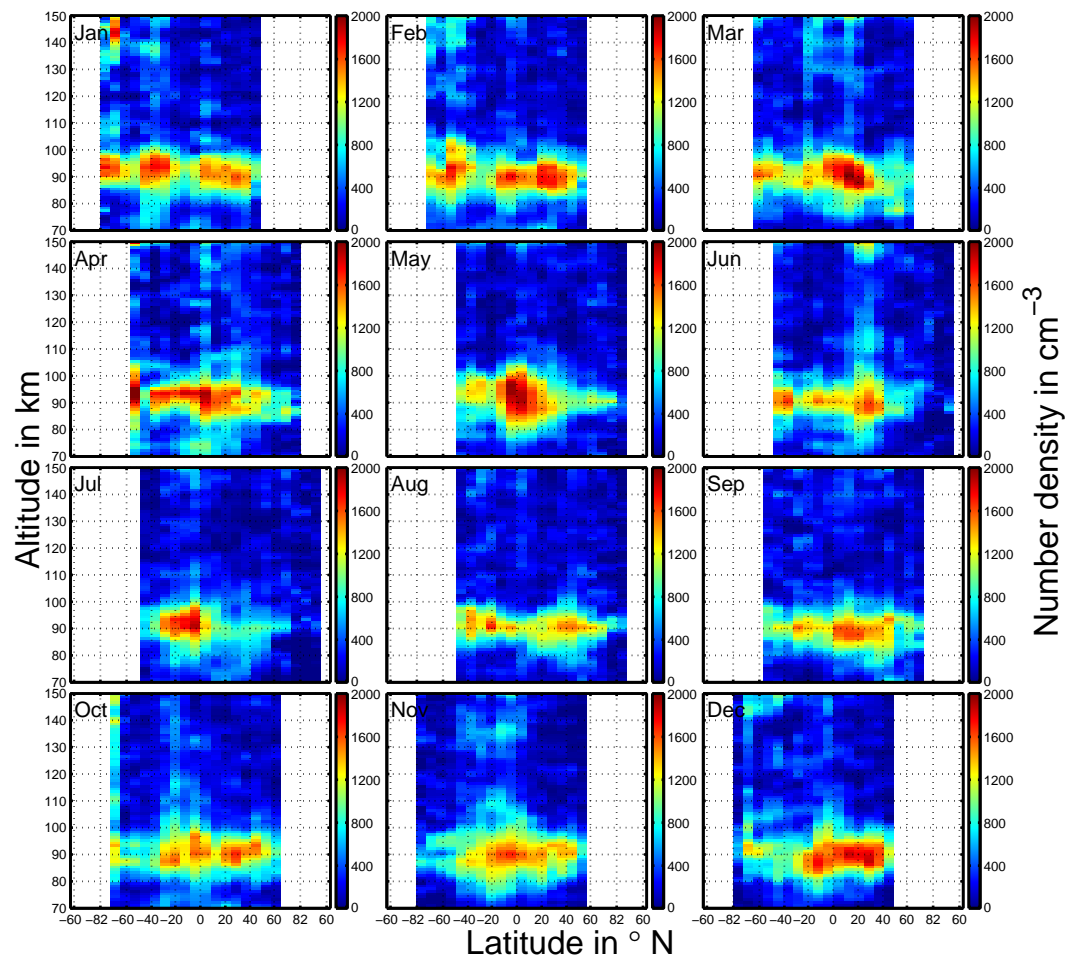


Fig. 5.1: Latitudinal variation of monthly (averaged over all January, February, etc. results from 2008-2012) and zonally averaged Mg density profiles retrieved from the 285.2 nm line. The Mg layer peaks around 90 km altitude and has a FWHM of about 15 km. Mg shows strong month-to-month variations, but there is no clear seasonal cycle to be observed.

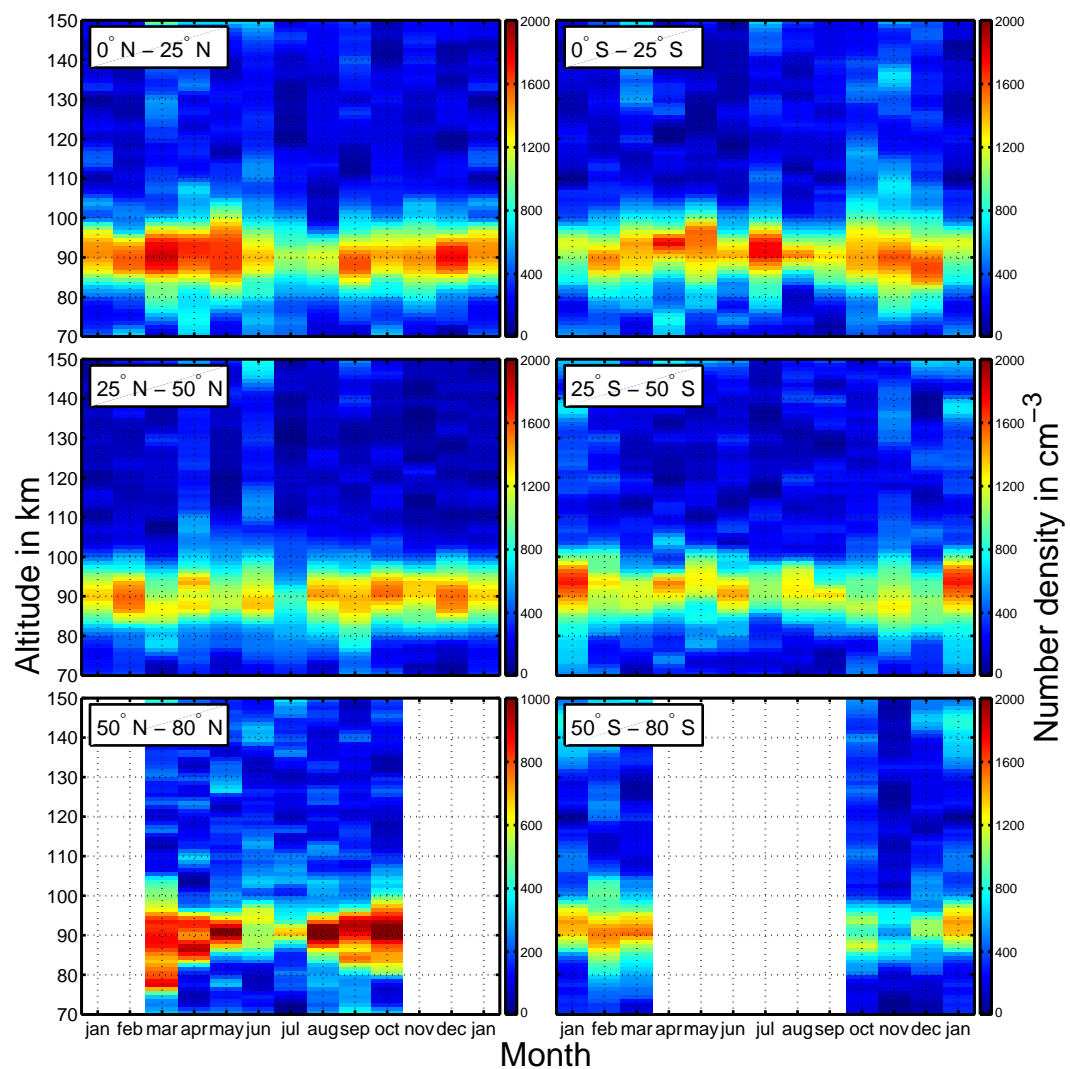


Fig. 5.2: Seasonal variation of the vertical Mg profile for different latitudinal zones (left: northern hemisphere, right: southern hemisphere, top: low latitudes, mid: mid latitudes, bottom: high latitudes). The peak altitude is at 90 km for all latitudes with variations of ± 5 km. The month-to-month variations in the peak altitude are bigger than any seasonal variations. The variations in the uppermost panels for the low latitudes may be interpreted as signs of the Mesospheric Semi-Annual Oscillation (MSAO).

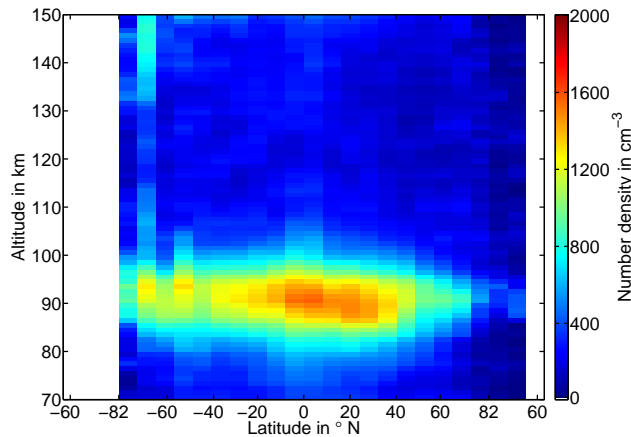


Fig. 5.3: Latitudinal variation of Mg profiles averaged over all available data for the years 2008-2012. Note that only between 45° N and S measurements from all 12 months contribute to the averages, while for high latitudes there is only summer coverage and/or near-terminator measurements.

Mg maxima occur at roughly 90 km altitude for all latitudes and this peak has roughly a FWHM of 15 km. There are strong day-to-day and also month-to-month variations for Mg. However, no clear seasonal cycle can be seen in the Mg MLT dataset and the variations most probably originate in the high statistical error for Mg. At low latitudes Mg shows signs of a semi annual oscillation. For high latitudes, which are only covered in summer, there are differences for the northern and southern hemisphere, with the northern hemisphere showing a depletion in density, while the southern hemisphere showing an increased density in the polar region. If it is not caused by noise, this may show a local time effect, because the southern hemisphere high latitudes are covered in morning local times, while the northern hemisphere high latitudes are covered in evening times. It is known that charged particles can travel along the magnetic field lines up to several earth radii, then become neutralized and sediment down on the night side. This Cleft Ion Fountain [13] may lead to this local time effect. It is also observed for Mg^+ . Note that at the time of this report, we were still doing checks to exclude instrumental issue to be the reason for the increased polar densities for Mg and Mg^+ above 100 km.

5.2 Results for Mg^+

Mg^+ has two emission lines which yield similar results. We only show results for the 279.6 nm line here. The 280.4 nm line yields nearly the same results as the 279.6 nm line. There are only minor differences between both, e.g. the 280.4 nm line showing slightly higher densities above the peak region. However, the key features are the same for both lines. Monthly mean results for Mg^+ are shown in figure 5.4 and the seasonal variations for different latitudinal zones are shown in figure 5.5. Figure 5.6 shows the mean result for the 4 years of the MLT dataset.

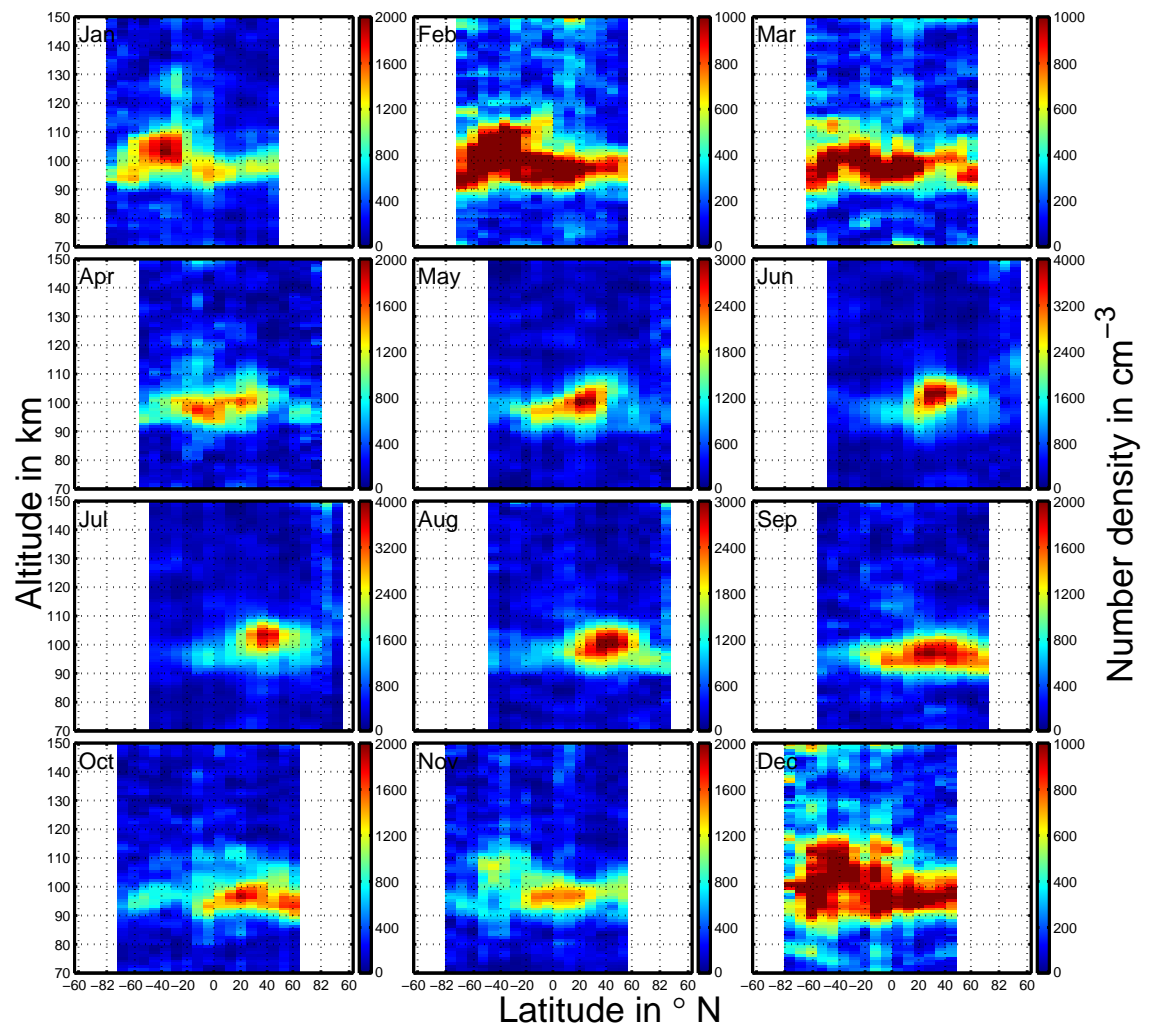


Fig. 5.4: Latitudinal variation of monthly and zonally averaged Mg^+ profiles (for the years 2008-2012) retrieved from the Mg^+ line at 279.6 nm. Mg^+ shows a seasonal cycle with a summer maximum, which is especially pronounced in the region between 25° and 45° latitude in the summer hemisphere. Furthermore, in this region the peak altitude is about 105 km, which is up to 10 km higher than at the equator or at the poles.

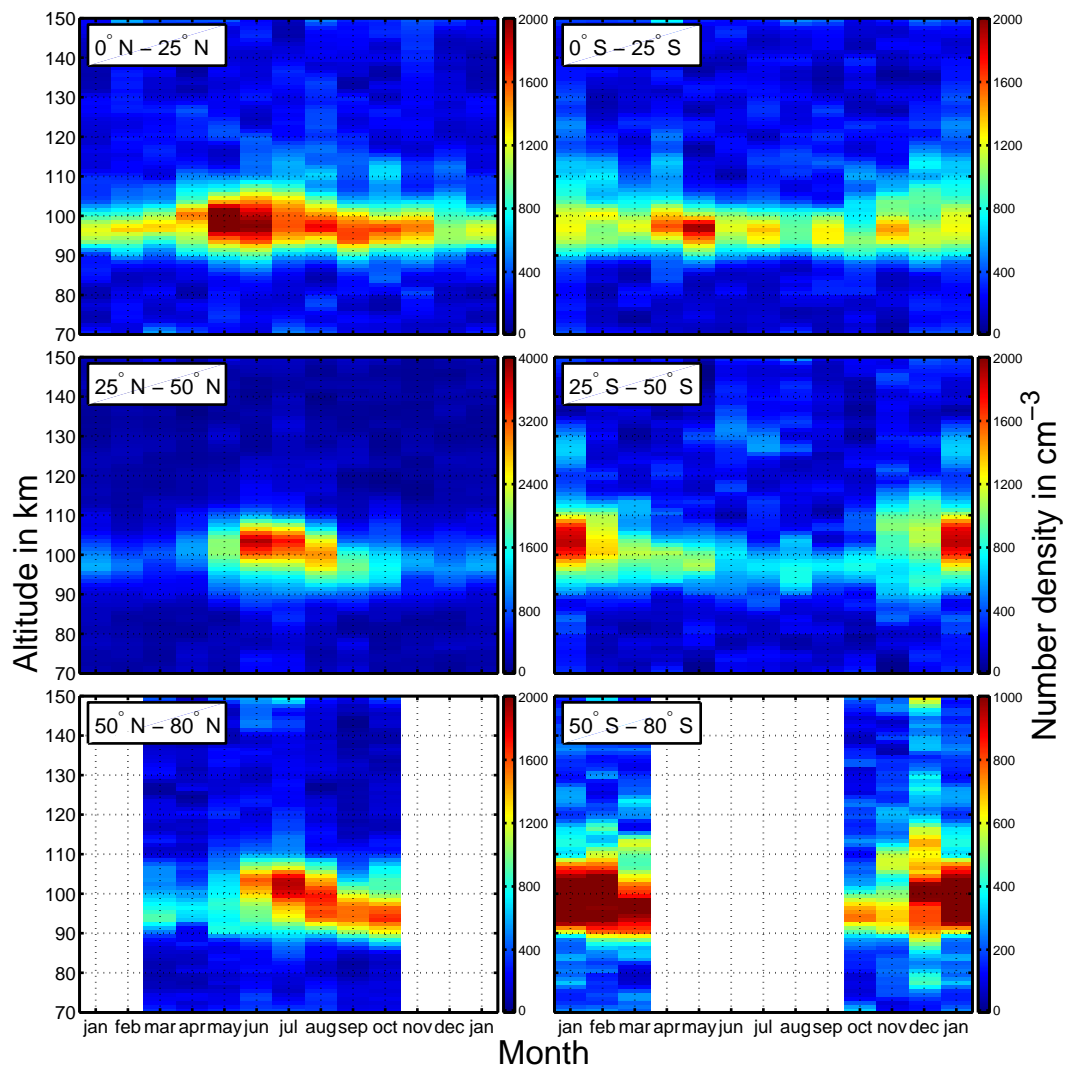


Fig. 5.5: Seasonal variation of the vertical profile of Mg^+ (279.6 nm line) for different latitudinal zones (left: Northern hemisphere, right: southern hemisphere, top: low latitudes, mid: mid latitudes, bottom: high latitudes), averaged over all available observations in 2008-2012. For all these latitudinal zones a seasonal cycle in the peak altitude with a summer maximum and a winter minimum can be observed. The seasonal variations are similar or larger than the month-to-month variations. The maximum peak altitude is 5-10 km higher than the minimum peak altitude. For mid latitudes, the peak altitude in the winter hemisphere is still higher than the peak altitude at the equator (see also Fig. 5.4).

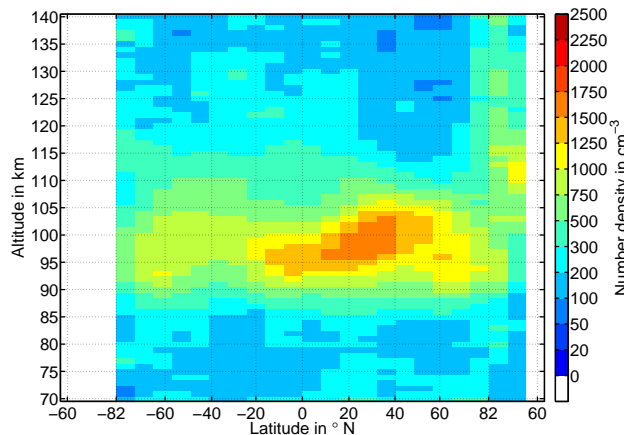


Fig. 5.6: Latitudinal variation of Mg^+ profiles averaged over all available data for 2008-2012 for the Mg^+ line at 279.6 nm. The result shows an asymmetric behavior between the northern hemisphere and the southern hemisphere with a higher densities in the northern hemisphere.

Mg^+ shows much less day-to-day variations than Mg. This most probably arises from the lower statistical error. Mg^+ shows a clear seasonal cycle with a summer maximum in peak density, which is most pronounced in mid latitudes. Furthermore, Mg^+ shows a clear latitudinal dependence in peak altitude with higher peak altitudes at mid latitudes than at the equator or the poles. This latitudinal dependence is overlapped by an additional seasonal dependence of the peak altitude, which has a summer maximum. The peak altitude at the equator is roughly 95 km, while the peak altitude between 20 and 40 degrees N can be up to 105 km. The FWHM of the peak is roughly 15 km, similar to the Mg layer. Further interesting features can be found when looking at the thermospheric content above the peak altitude. For the equatorial and polar regions densities above 120 km are higher than for the mid latitudes. A vertical transport mechanism in the thermosphere explains this feature. Strong vertical transport reduces the densities at the top of the ion layer, which effectively increases the densities above the layer and decreases the peak altitudes. Another reason for the steep gradient in the layers altitude may be, that the neutral meridional wind, directing into the summer hemisphere in the thermosphere, leads to a transport to latitudinal regions where the vertical transport is suppressed, which increases the peak altitude at mid latitudes. For the polar regions the Cleft Ion Fountain effect [13] (discussed in the Mg section) may explain the high densities at high northern polar latitudes during the evening. At least it is consistent to see high densities for Mg^+ in the evening showing upward transport of the ions and to see high Mg densities in the morning, showing the downward transport. This, however, can only be observed at different poles. For the equatorial region a suitable vertical transport mechanism is described in [6].

5.3 Results for Na

The Na D1 and D2 lines lie in the visible wavelength region and have a high signal to noise ratio compared to the Mg and Mg^+ lines. Therefore seasonal variations are much easier to detect and other issues, e.g. the strong sensitivity of the Mg/ Mg^+ retrieval to

smoothing constraints vanish. However, as discussed in section 4.3 the estimation of the additional actinic flux from multiple scattering brings an additional issue into the retrieval algorithm for Na. For this study different constant albedo factors for all latitudes have been tested and overall a factor 1.6 led to the best match of the D1 and D2 line, which yielded maximum densities of roughly 4000 cm^{-3} for most monthly averages. A test with a high albedo factor of 2.5 yielded typical maximum densities of roughly 3000 cm^{-3} for D1 and 2000 cm^{-3} for D2, while for a low albedo factor of 1.0 the peak densities are up to 8000 cm^{-3} for D1 and 10000 cm^{-3} for D2. The densities for the less sensitive line D1 $3000\text{--}8000 \text{ cm}^{-3}$ can be assumed to limit the maximum range of variation, and both numbers are in the same order of magnitude. In the following, only the results using the factor 1.6 are presented.

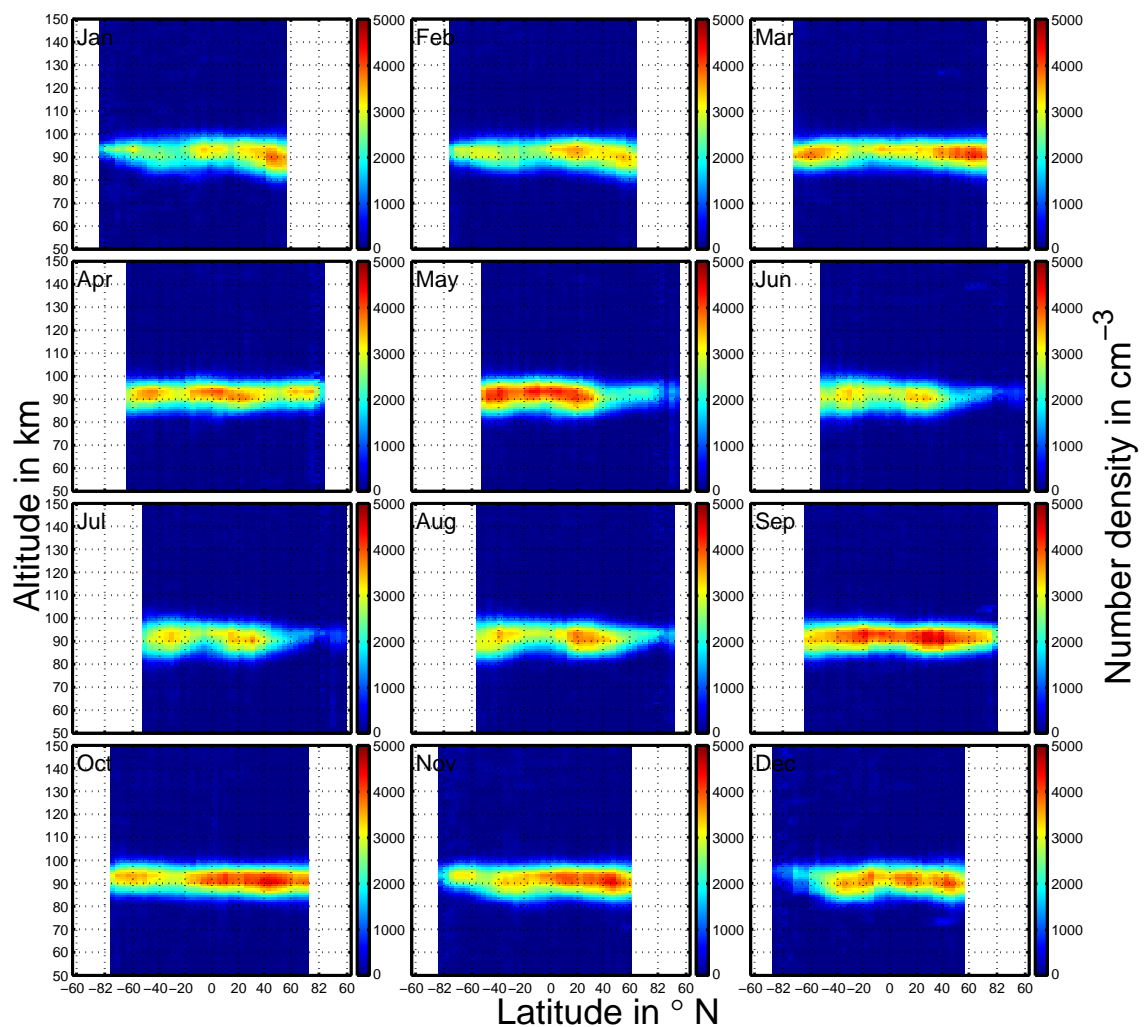


Fig. 5.7: Na number densities versus latitude and altitude for monthly mean results 2008-2012, retrieved from the Na D1 line. A clear depletion of Na can be observed at the summer pole.

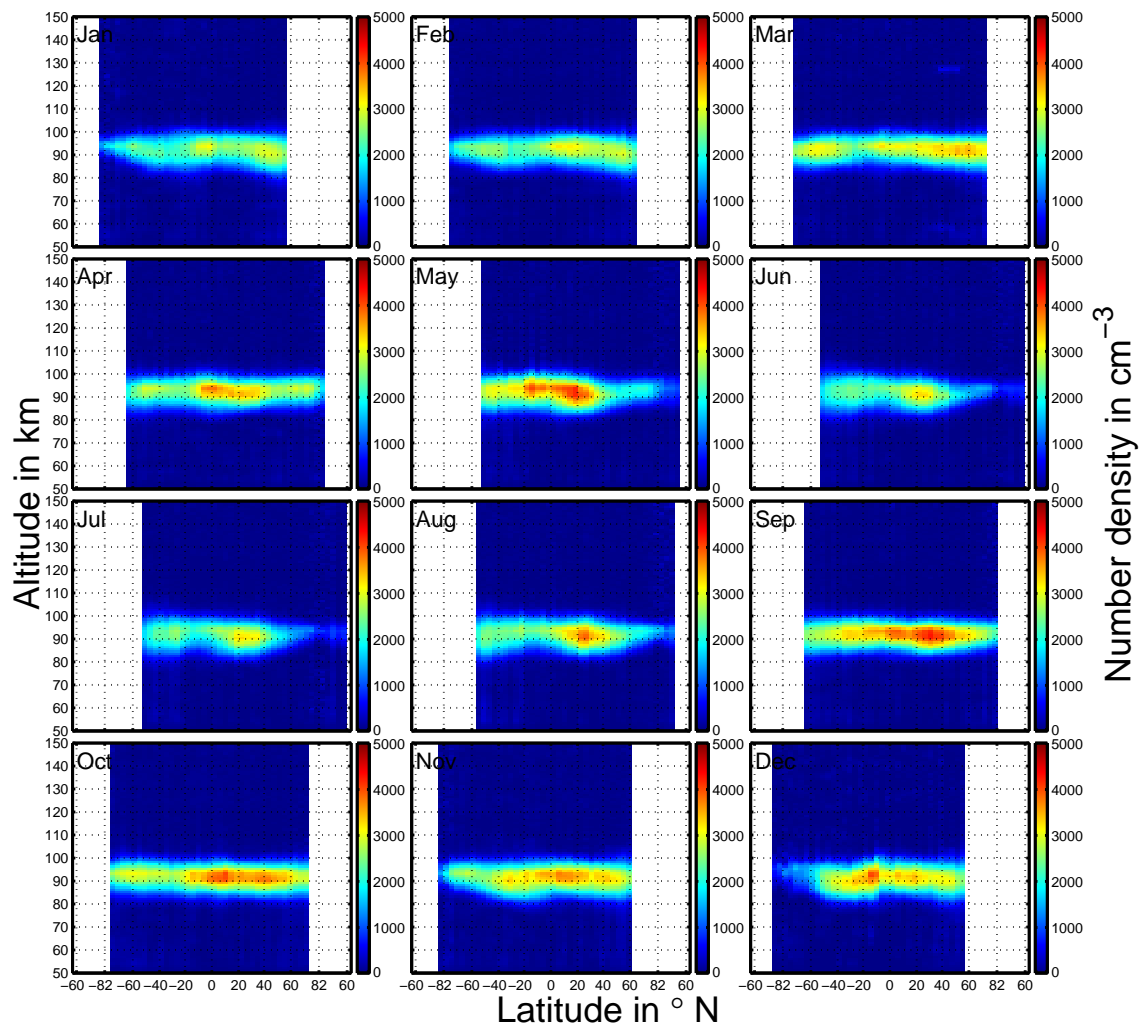


Fig. 5.8: Na number densities versus latitude and altitude for monthly mean results 2008-2012, retrieved from the Na D2 line. A clear depletion of Na can be observed at the summer pole.

Figures 5.7 and 5.8 show monthly means for Na retrieved from the D1 line and the D2 line, respectively. The peak altitude is nearly constant at roughly 92 km for all latitudes. For the result of the D1 line the density is nearly constant at nearly all latitudes, beside for the high latitudes, where a strong depletion of density can be observed in the summer. Differences between the D1 and D2 line results are shown in figure 5.9. The D2 densities are often higher than the D1 densities above and below the peak altitude, while at the peak altitude the D1 density is higher, so the D2 line shows a wider vertical profile.

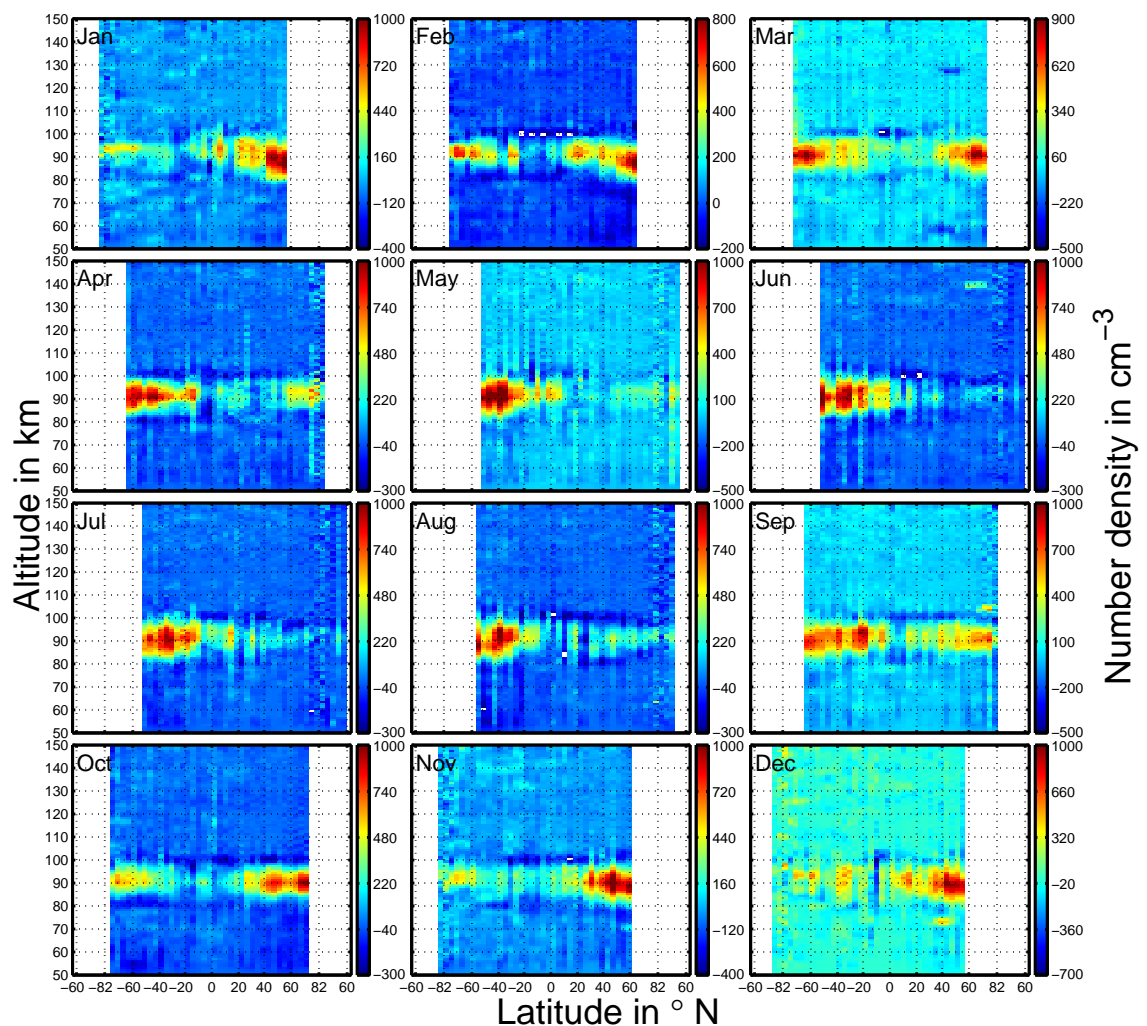


Fig. 5.9: Densities of Na retrieved from the D1 line minus densities retrieved from the D2 line. In the peak altitude D1 densities are larger than D2 densities at the left and right edge of the plots (independently from the latitude). Furthermore, the D2 densities are larger above and below the peak region, while D1 is larger at the peak altitude, so effectively the D2 vertical profile is wider than the D1 vertical profile.

In the peak region these plots show increased densities for D1 at the left and right edges (begin and end of the orbit). This feature is well correlated with phase function variations and variations of the solar zenith angle (SZA). As a next step solution an albedo factor will be used, which takes into account those variations and modulates the albedo factor, e.g. by $\cos(SZA)$ or a similar function. Later, this function can be used as an alternative solution for measurements, where the albedo factor finding algorithm described in section 4.3 fails.

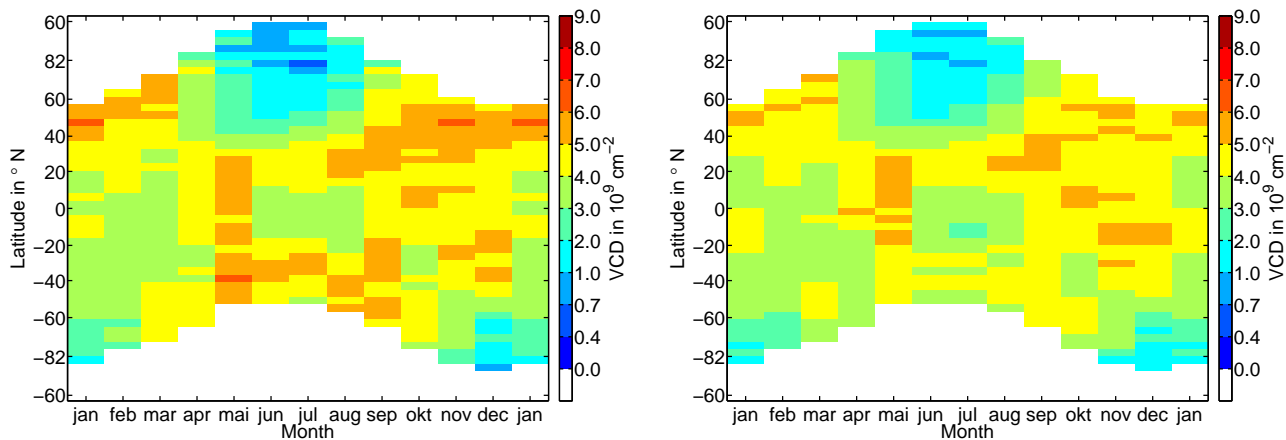


Fig. 5.10: Vertical column densities of Na retrieved from the D1 line (left) and the D2 line (right) versus latitude and month.

Figure 5.10 shows the variation of the VCDs with latitude and month. This result is in good agreement with results from other instruments (e.g.[9]) and models (e.g.[14]), with the D1 line showing the slightly better agreement.

5.4 Other metals

We also investigated other possible emission lines for metal atoms and ions using the 4 year averaged spectra of the MLT states at the equator. The strongest Fe line was expected to be at 248 nm. However, this line is rather weak and overlaps with strong nearby NO lines, which made the background subtraction complicated, so that even from the 4 year averaged spectra no reasonable Fe profile could be retrieved. Similar issues occurred at several other wavelengths below 305 nm (e.g. 252, 272 and 302 nm). Emission signals have been found for the 372 nm and the 386 nm line, where the 386 nm appeared to be too noisy to be investigated. The 372 nm line shows a clear emission signal and using the same Ring effect correction as for the Mg/Mg⁺ lines yielded a good SCD profile and an at first glance reasonable density profile. However, this profile has several issues. On the one hand side the densities are already in the right order of magnitude, although the low resolution solar spectrum of SCIAMACHY was used for the solar irradiance value. Experiences with the other Fraunhofer lines yield, that the density would be at least a factor 3 bigger, when using a high resolution spectrum of the line. Furthermore, no self absorption correction was applied, which further increases the density. The more severe issue with the 372 nm line, however, is that there are 3 other nearby Fe lines, which are not ground state transitions and should not be in the same order of magnitude as the ground state transition, since they yield densities of excited states. The strengths of these nearby lines points to strong filling in of the lines by single and multiple scattering. Multiple scattering is strong in this wavelength region, because the ozone absorption cross section has a minimum there and there are also no other strong absorbers. We think, that just correcting the single scattering Ring effect leads to a wrong profile, which is most probably formed to a large extent by inelastic multiple scattering, which however, looks dangerously reasonable. Figure 5.11 shows the retrieved density profile, as well as the 4 strong emission lines in the 372 nm

region.

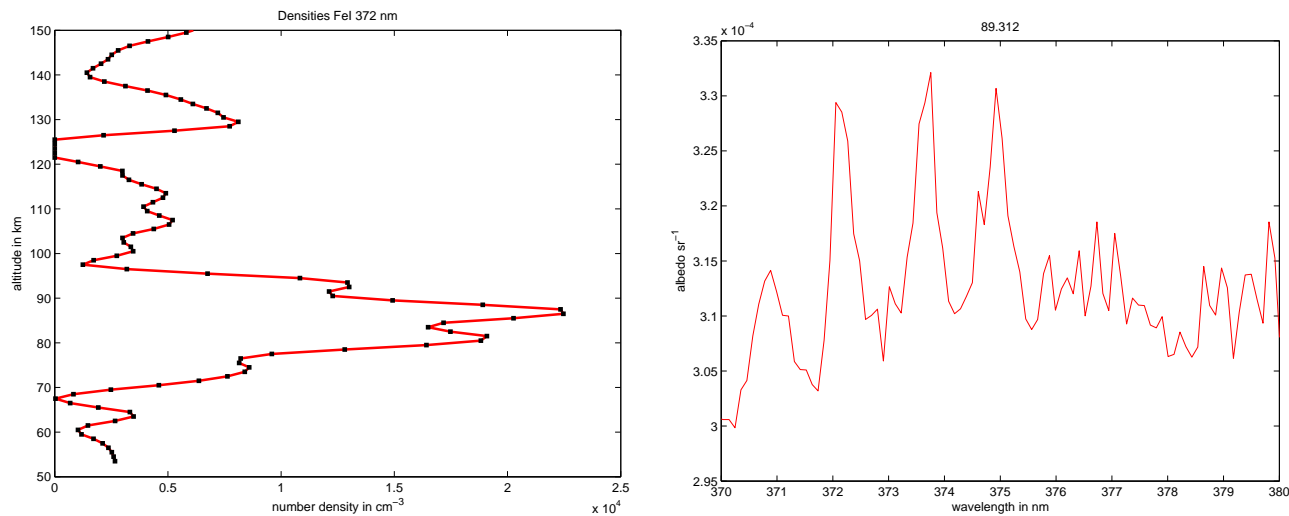


Fig. 5.11: Retrieved number densities of Fe (left; 40° N, October 6 2009). The vertical density profile looks reasonable with a peak altitude of 90 km and peak densities in the order of 20000 cm⁻³. The right figure shows the spectrum at 89.3 km altitude. Beside the line at 372 nm (second from left) 3 other strong lines can be seen, which, however, are not ground state transitions. These lines are most probably formed by the multiple scattering Ring effect, rather than by metal emissions.

Similar issues as for the Fe line at 372 nm can also be observed for the Ca⁺ lines at 393 and 396 nm. The Ca line with the highest emissivity is at 422 nm. However, even for the 4 year average this line can hardly be seen in the equatorial region. The K line at 770 nm seems to be the most promising other metal line in the SCIAMACHY spectrum. This line shows a clear emission peak in the right altitude range. However, it is close to the O₂-A band emission lines at 760 nm, which are much stronger than the K line and occur as emission lines below 110 km and as absorption lines above 118 km, which makes the background treatment complicated. However, successful retrievals from a similar satellite experiment for K was most recently reported by [5]. FeO emission features in the vicinity of the Na lines at around 590 to 600 nm are observed, as the only molecular emission feature so far. A slide showing all strong emission lines in the SCIAMACHY limb spectrum is appended to the report.

6 Conclusions

Spectra from the SCIAMACHY limb MLT measurements (2008-2012) have been used in this project, to retrieve number densities for several metal atom and ion species (Mg, Mg⁺ and Na). Furthermore, the retrieval algorithm has been significantly improved. A Ring effect correction has been added to the retrieval algorithm, as well as a treatment of self absorption. High resolution features in the spectra, like fully resolved Fraunhofer lines in the solar spectrum, spectral shifts and splittings due hyper-fine structure, Doppler effect

and isotopic compositions are now considered in the algorithm. As a result, the Mg vertical profiles do not show a second maximum at 70 km anymore and through the improved resolution in the peak region of the metal atom and ion layers a clear latitudinal dependence of the Mg^+ peak altitude could be observed for the first time. Furthermore, a treatment of multiple scattering effects extended the retrieval algorithm to derive Na densities. Knowing the global mesospheric metal density distribution, combined with models, including reaction rates of loss processes as well as the meteoric composition and fraction ablated in the upper atmosphere, will make it possible to estimate the daily input of meteoric material to the earth atmosphere. The knowledge won from the MLT dataset can be used to reanalyze the nominal limb and nadir dataset, e.g. as a priori information in the retrieval and the potential of the SCIAMACHY dataset is still not fully exhausted. An accurate neutral and ionized metals global data set is now available for the period 2008 to 2012. These data have been compared with a 2D photochemical/dynamical model for Mg and Mg^+ showing that there are differences between model and data for Mg on a seasonal basis even though Mg^+ model and data are in agreement. The data show clearly significant transport of both Mg and Mg^+ above 100 km in both the polar and equatorial regions. In addition to providing a global data set for Mg and Mg^+ and Na, the present effort has demonstrated the algorithm necessary to yield the global distribution of other metal species such as Fe. Such an effort should be carried out. In addition, data should be compared with a global model of the ionospheric E region. This model should be global and include electrodynamic transport. Additional data sets such as NO from SCIAMACHY and TIMED data would enhance the study.

7 Acknowledgements

We wish to thank EOARD for funding this project and the Window on Science program support for the travel to two conferences in New Mexico in 2011. We thank the project managers and administrator at EOARD for their helpful support of such fundamental upper atmospheric science.

References

- [1] A. C. Aikin and R. A. Goldberg. Metallic ions in the equatorial ionosphere. J. Geophys. Res., 78:734 – 745, 1973.
- [2] S. Bender, M. Sinnhuber, J. P. Burrows, M. Langowski, B. Funke, and López-Puertas. M. Retrieval of nitric oxide in the mesosphere and lower thermosphere from sciamachy. Atm. Meas. Tech., 6:2521 – 2531, 2013.
- [3] Z. Ceplecha, J. Borovička, W. G. Elford, D. O. Reville, R. L. Hawkes, V. Porubčan, and M. Šimek. Meteor phenomena and bodies. Space Science Reviews, 84:327 – 471, 1998.
- [4] J. Correia, A. C. Aikin, J. M. Grebowsky, and J. P. Burrows. Metal concentrations in the upper atmosphere during meteor showers. ACP, 10(3):909 – 917, 2010.

- [5] E. Dawkins. Metals in the mesosphere: Meteoroids, satellite retrievals and modelling. 11th Layered Phenomena in the Mesopause Region Workshop, Leeds, UK, 29 July - 1 August, 2013.
- [6] C. G. Fesen, P. B. Hays, and D. N. Anderson. Theoretical modelling of low-latitude mg^+ . J. Geophys. Res., 88:3211 – 3223, 1983.
- [7] G. Flynn. Chapter 4 in: Meteors in the Earth’s atmosphere edited by Murad, E. and Williams, I. P.,. Cambridge University Press, Cambridge, 2002.
- [8] J.F. Grainger and J. Ring. Anomalous fraunhofer line profiles. Nature, 193:762, 1962.
- [9] J. Hedin and J. Gumbel. The global mesospheric sodium layer observed by odin/osiris in 2004-2009. J. of Atmos. and Sol.-Terr. Phys., 73(14-15):2221 – 2227, 2011.
- [10] W. Huang. Simultaneous and common-volume lidar observations of mesospheric na and fe layers at boulder colorado (40n, 105w) in 2010. Joint CEDAR/GEM Workshop 2011, Santa Fe, NM, 26.6.-1.7., Poster MLTL-04, 2011.
- [11] M. Langowski, M. Sinnhuber, A.C. Aikin, C. von Savigny, and J. P. Burrows. Retrieval algorithm for densities of mesospheric and lower thermospheric metal and ion species from satellite borne limb emission signals. Atm. Meas. Tech. Disc., 6:4445 – 4509, 2013.
- [12] M Langowski, C. von Savigny, J. P. Burrows, W. Feng, J. M. C. Plane, D. R. Marsh, D Janches, M Sinnhuber, and A. C. Aikin. Global mg and mg ion observation between 70 km and 150 km with sciamachy/envisat. J. of Atmos. and Sol.-Terr. Phys., to be submitted.
- [13] M. Lockwood, J. R. Horwitz, M. O. Chandler, J. H. Waite, T. E. Moore, and C. R. Chappel. The cleft ion fountain. J. Geophys. Res., 90:9736 – 9748, 1985.
- [14] D. R. Marsh, D. Janches, W. Feng, and J. M. C. Plane. A global model of meteoric sodium. J. Geophys. Res- Atmos., page in press, 2013.
- [15] D. Nesvorný, P. Jenniskens, H. F. Levison, W.F. Bottke, D. Vokrouhlický, and M. Gounelle. Cometary origin of the zodiacal cloud and carbonaceous micrometeorites. implications for hot debris disks. Astrophys. J., 713:816 – 836, 2010.
- [16] J. M. C. Plane. Cosmic dust in the earth’s atmosphere. J. of Atmos. and Sol.-Terr. Phys., 41:6507 – 6518, 2012.
- [17] J. M. C. Plane and M. Helmer. Laboratory study of reactions $\text{mg} + \text{o}_3$ and $\text{mgo} + \text{o}_3$, implications for the chemistry of magnesium in the upper atmosphere. Faraday Discuss., 100:411 – 430, 1995.
- [18] V. V. Rozanov, A. V. Rozanov, A. A. Kokhanovsky, and Burrows J. P. Radiative transfer through terrestrial atmosphere and ocean: Software package sciatran. J. Quant. Spect. Rad. Trans., in Press, <http://dx.doi.org/10.1016/j.jqsrt.2013.07.004>, 2013.

- [19] M. Scharringhausen. Investigation of mesospheric and thermospheric magnesium species from space. Ph.D. thesis, 2007.
- [20] T. Vondrak, J. M. C. Plane, S. Broadley, and D. Janches. A chemical model of meteoric ablation. *ACP*, 8:7015 – 7031, 2008.

8 Conference Contributions

Langowski et al., Satellite Remote Sensing of Metals and Metal Ions in the upper Mesosphere and lower Thermosphere with SCIAMACHY/Envisat, oral presentation, AFOSR Space Sciences Program Review, Albuquerque, NM, 23-24 June 2011

Langowski et al., Satellite Remote Sensing of Mg and Mg⁺ in the mesosphere and lower thermosphere by satellite remote sensing using data from SCIAMACHY/Envisat, poster MLT-MLTS-08, CEDAR/GEM conference, Santa Fe, NM, 26 June - 1 July 2011

Langowski et al., Satellite Remote Sensing of Metals and Metal Ions in the upper Mesosphere and lower Thermosphere with SCIAMACHY/Envisat, oral presentation, Advances in Atmospheric Sciences (ATMOS), Bruges, Belgium, 18-22 June 2012

Langowski et al., Mg and Mg⁺ retrieval results from SCIAMACHY limb mesosphere-thermosphere measurements, oral presentation, 7th Atmospheric Limb Conference, Bremen, Germany, 17-19 June 2013

Langowski et al., Mg and Mg⁺ retrieval results from SCIAMACHY limb mesosphere-thermosphere measurements, oral presentation, 11th Layered Phenomena in the Mesopause Region Workshop, Leeds, United Kingdom, 29 July - 1 August 2013

Langowski et al., Metal Retrievals in the Mesosphere and lower Thermosphere by remote Sensing of Airglow with SCIAMACHY/Envisat, poster SA11B-1923, American Geophysical Union's 46th annual Fall Meeting, San Francisco, CA, 9-13 December 2013

9 List of Symbols, Abbreviations, and Acronyms

AMT – Atmospheric Measurement Techniques
 AMTD – Atmospheric Measurement Techniques Discussions
 Envisat – Environmental Satellite
 ESA – European Space Agency
 FWHM – full width at half maximum
 iFOV – instrumental field of view
 MLT – mesosphere and lower thermosphere
 LFS – line from sun
 LOS – line of sight
 PMC – polar mesospheric cloud
 PSC – polar stratospheric cloud

SCD – slant column density

SCIAMACHY – Scanning Imaging Absorption Spectrometer for Atmospheric CHartography, greek “Fighting shadows”

SCIATRAN – radiative transfer model and retrieval algorithm, see <http://www.iup.uni-bremen.de/sciattran/>

TIMED – Thermosphere Ionosphere Mesosphere Energetics and Dynamics is an orbiter mission dedicated to study the dynamics of the MLT portion of the Earth’s atmosphere

SZA – solar zenith angle

VCD – vertical column density

10 Appendix A

Sketch of emission lines covered by SCIAMACHY. The plots show limb radiances divided by the solar irradiance for the 4 year average of the MLT dataset at the equator.

